Understanding the large shift photocurrent of WS_2 nanotubes: A comparative analysis with monolayers

Jyoti Krishna,[1] Peio Garcia-Goiricelaya,[1] Fernando de Juan,[2,3] and Julen Ibañez-Azpiroz[1,2,3]
[1]*Centro de Física de Materiales (CSIC-UPV/EHU), 20018, Donostia-San Sebastián, Spain*
[2]*Donostia International Physics Center (DIPC), 20018 Donostia-San Sebastián, Spain*
[3]*Ikerbasque Foundation, 48013 Bilbao, Spain*

(Received 26 July 2023; revised 26 September 2023; accepted 5 October 2023; published 23 October 2023)

We study the similarities and differences in the shift photocurrent contribution to the bulk photovoltaic effect between transition-metal dichalcogenide monolayers and nanotubes. Our analysis is based on density functional theory in combination with the Wannier interpolation technique for the calculation of the shift photoconductivity tensor. Our results show that for nanotube radii of practical interest, $r > 60$ Å, the shift photoconductivity of a single-wall nanotube is well described by that of the monolayer. Additionally, we quantify the shift photocurrent generated under realistic experimental conditions like device geometry and absorption capabilities. We show that a typical nanotube can generate a photocurrent of around 10 nA, while the monolayer only attains a maximum of 1 nA. This enhancement is mainly due to the larger conducting cross section of a nanotube in comparison to a monolayer. Finally, we discuss our results in the context of recent experimental measurements on WS_2 monolayer and nanotubes [Zhang *et al.*, Nature (London) **570**, 349 (2019)].

DOI: 10.1103/PhysRevB.108.165418

I. INTRODUCTION

The bulk photovoltaic effect (BPVE) offers a promising alternative to traditional solar cells thanks to its ability to generate a dc current upon light absorption in homogeneous materials. This effect is described as a second-order optical process; hence, it can only take place in crystal structures that break inversion symmetry [1,2]. The photovoltage attained in the BPVE is not limited by the band gap of the material, giving rise to large measured values [3,4].

Recently, the study of the BPVE, and, in particular, the shift-current contribution, has witnessed reinvigorated interest [5–8]. While traditionally this effect has been mostly studied in bulk ferroelectrics such as $BaTiO_3$ [9,10], recent theoretical works have emphasized that the shift current undergoes a significant enhancement in two-dimensional (2D) systems such as single-layer monochalcogenides [11,12]. Current efforts include searching for suitable crystal structures with 2D-like properties, in the hope that they may yield an efficient harvesting of light [13,14].

In this context, *nanotubes*, which consist of a stack of rolled monolayers, offer an ideal bridge between a purely 2D system and a bulk crystal structure. Early theoretical work by Král *et al.* [15] showed the possibility of generating a net shift current in acentric and polar BN nanotubes. In addition to the quasiparticle contribution, the role of excitons (collective excitations composed by electron-hole pairs) in enhancing the nonlinear light-absorption process has also been addressed [16,17]. Low-dimensional transition metal-dichalcogenides (TMDs) also show very good potential as solar-cell devices due to their capacity to absorb a substantial amount of light in the visible range [14], and they are also ideal platforms to study van der Walls interactions and excitonic effects, among other phenomena [18]. Interestingly, a recent experiment on WS_2 TMD nanotubes reported a short-circuit current of around 10 nA [19], yielding one of the largest figure-of-merit reported to date for nonlinear processes. This remarkable value may find its origin on the shift-current contribution [20], which is allowed by the lack of inversion symmetry of these TMD polytypes.

In this paper, we perform a systematic study of the shift current in WS_2 monolayer and nanotube structures to discern the similarities and differences between the two. Our analysis is based on *ab initio* density functional theory (DFT) in combination with Wannier-interpolation techniques for an efficient and accurate calculation of the shift photoconductivity tensor [21]. We find that the optical properties of a single-wall nanotube are well described by those of a monolayer for nanotube radii larger than ∼60 Å, which is generally the range of practical interest. While the shift photoconductivity of the nanotube is somewhat modified by interactions between walls for typical interwall distances, we do not find a substantial and systematic enhancement. Despite possessing a similar shift photoconductivity, we show that a WS_2 nanotube can generate a photocurrent of around 10 nA, while the monolayer attains a maximum photocurrent of order 1 nA. Finally, we compute the angular current distribution of both nanotube and monolayer and compare it with the one recently measured in experiment [19].

The paper is organized as follows. In Sec. II. we discuss technical details regarding the approach to describe the monolayer and nanotube structures and the calculation of optical responses using Wannier interpolation. In Sec. III, we show the bulk of our results; after a brief comment on symmetry considerations (Sec. III A), we analyze the calculated optical photoconductivies of monolayer and nanotube structures

(Sec. III B) and the generated dc photocurrent (Sec. III C). Finally, in Sec. IV, we provide the main conclusions, and supplementary calculations are included in the Appendix.

II. METHODS

We have performed first-principles calculations using DFT as implemented in the SIESTA code package [22]. We have used norm-conserving pseudopotentials [23,24] and we have treated exchange-correlation effects by means of the local density approximation [25,26]. We have used a basis set centered at the transition metal (M) and chalcogen (X) atoms of the double-zeta type with polarization orbitals, and we have tested that the results are virtually unchanged using triple-zeta plus polarization orbitals.

We have considered the trigonal 2H-phase crystal structure [27] for modeling TMD monolayers of stoichiometry MX_2. Then, by choosing a three-atom fundamental unit domain (one M sandwiched between two X's), we have constructed a single-wall nanotube by rolling up the 2D monolayer along the chiral vector $\vec{C}$ defined as $\vec{C} = n\vec{a} + m\vec{b}$, where $\vec{a}$ and $\vec{b}$ are lattice unit vectors of the monolayer and the chiral (integer) indexes (n, m) determine the chirality of the nanotube. In this paper, we have focused on the so-called zigzag nanotubes of the type $(n, 0)$ [see Fig. 1(d)]. For large $n > 15$, the nanotube radius r is proportional to $n/2$. In our calculations, we have considered the range $r \in [10 - 60]$ Å, and we have incorporated a vacuum region of more than 15 Å in every nonperiodic direction of the computational slab to avoid spurious interactions among the periodic images. Accordingly, we have sampled the Brillouin zone using a Γ-centered **k**-mesh of $15\times15\times1$ for the monolayer, $10\times1\times1$ for the single-wall nanotube, and $5\times1\times1$ for the double-wall nanotube with mesh cutoff energy of 100 Ry used in all the calculations.

In a postprocessing step, we have calculated maximally localized Wannier functions (MLWFs) [28,29] from a set of Bloch states, using the WANNIER90 code package [30]. For the monolayer, we have constructed 11 MLWFs comprising seven high-energy valence bands and four low-energy conduction bands using d and p orbitals centered on M and X ions, respectively. For the nanotube, we have constructed the MLWFs by choosing the localized sets of valence and conduction bands around the Fermi level that comprise the d and p orbitals centered on all the M and X ions in the slab, which depends on the chiral index n.

Finally, we have computed the linear (σ_1^{aa}) and shift-current (σ_2^{abb}) photoconductivities using the Wannier-interpolation technique implemented in the `postw90` module [30]. We have computed the dipole matrix element and its covariant derivative entering the expression for the transition matrix elements [31] following the approach of Refs. [32] and [21], respectively. We employed an interpolation **k** mesh and energy smearing width of $10000\times10000\times1$ and 0.02 eV for the monolayer, respectively, and $1000\times1\times1$ and 0.03 eV for the nanotubes, respectively.

III. RESULTS

A. Symmetry considerations

2D TMD monolayers MX_2 are formed by a trigonal prismatic network of M transition metal atoms sandwiched by two inequivalent X chalcogen atoms, as illustrated in Figs. 1(b) (side view) and 1(c) (top view). The system breaks inversion symmetry but is symmetric under $y \to -y$ with a mirror-symmetry plane M_{xz} denoted in Fig. 1(c). The point group of the system is D_{3h}, and the symmetry-allowed components of the shift photoconductivity tensor σ^{abc} are $xxx = -xyy = -yyx = -yxy$ (only one independent component).

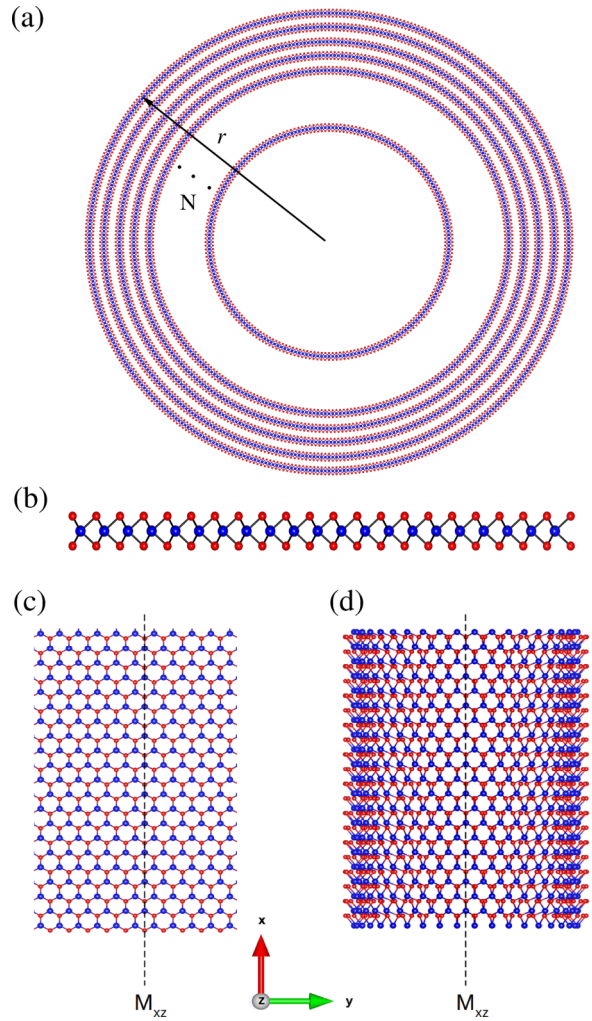

FIG. 1. Side view of two TMD MX_2 structures: (a) Multiwall zigzag nanotube of radius r composed of N layers and (b) 2D hexagonal monolayer. (c), (d) The corresponding top views for monolayer and a single wall nanotube, respectively. The mirror-symmetry plane M_{xz} is denoted by a dashed black colored line. The M and X atoms are shown as blue and red balls, respectively.

Regarding the nanotube structure, in this paper we will report results on the so-called zigzag configuration, as we have checked (see Appendix) that other configurations such as armchair and chiral ones yield similar or slightly smaller optical absorption (this is in line with Ref. [20]). A zigzag nanotube belongs to the isogonal point group C_{2nv} [33] (n denotes a positive integer number), which contains rotations around the tube axis X and vertical mirror planes such as the one illustrated in Fig. 1(d). The symmetry-allowed tensor components of the shift current are xxx and $xyy = xzz$ (two independent components). In practice, this implies that the

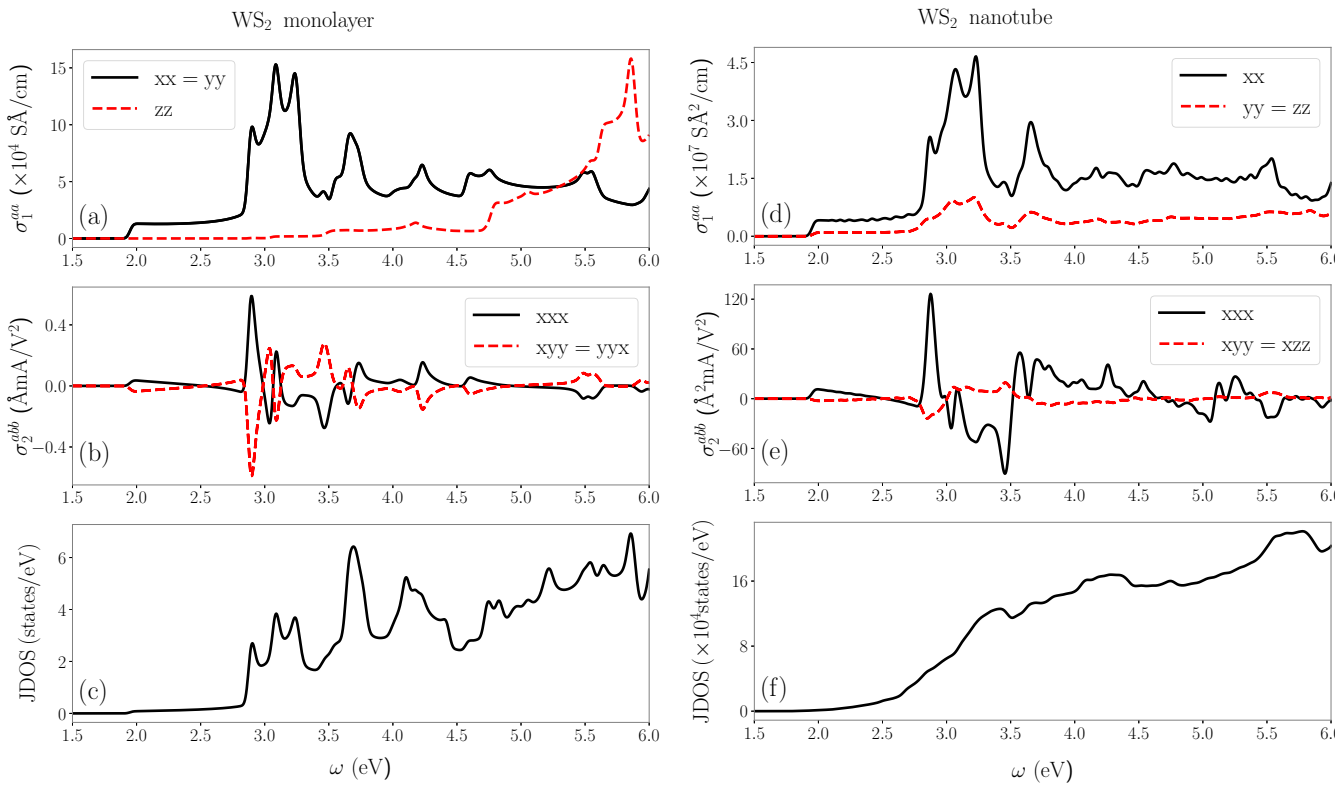

FIG. 2. Symmetry-allowed tensor components of linear (σ_1^{aa}) and shift (σ_2^{abb}) photoconductivity versus photon frequency (in eV) of WS_2 monolayer [(a), (b), respectively] and a single-walled zigzag nanotube of $r = 50$ Å [(d), (e), respectively]. (c), (f) The respective optical joint density of states (JDOS) of monolayer and nanotube.

photocurrent flows only along the direction of the tube axis, irrespective of the light polarization.

B. Linear and shift current photoconductivity

1. Monolayer and single-wall nanotube

We begin our analysis by studying the linear and shift photoconductivity of WS_2 in various forms. Let us start by describing the calculated results for the monolayer, shown in Figs. 2(a) and 2(b) together with the corresponding joint density of states (JDOS) in Fig. 2(c), which provides a measure of allowed interband optical transitions [21,34]. As expected, the peaks in the various linear and shift photoconductivity spectra coincide with the peaks in the JDOS. Focusing on the shift current, the maximum value takes place at $\simeq 2.9$ eV, where it reaches 0.57 Å mA/V^2. As prescribed in Ref. [11], dividing this figure by the monolayer thickness $l = 3.14$ Å one can obtain an estimated bulk value of about 180 μA/V^2. This value is significantly larger than the the shift photoconductivity of prototypical ferroelectrics and perovskites [5,35,36], and is in line with values reported in other 2D monolayers such as GeS [12].

We turn now to analyze the optical properties of a single-wall nanotube of radius $r = 50$ Å. The calculated band gap $\simeq$ 1.9 eV is very close to that of the monolayer value (see electronic band structures in the Appendix), in line with previously reported values [37,38]. For both the linear [Fig. 2(d)] and shift current [Fig. 2(e)] spectra, the dominant photoconductivity component corresponds to the tube axis σ_1^{xx} and σ_2^{xxx}, respectively. In both cases, the shapes are very similar to the associated components calculated for the monolayer, and the maximum shift current reaches 120 Å^{2}mA/V^2. Note, however, that due to the difference in units between Figs. 2(b) and 2(e), a direct quantitative comparison between monolayer and nanotube shift photoconductivity is not straightforward.

To overcome this subtlety, we have opted for considering a quantity known as the *shift distance*. This magnitude quantifies the real-space distance traveled by electronic carriers upon photoexcitation as a consequence of the shift-current mechanism [39]. It is defined as

$$D^{abb} = \frac{\hbar}{\epsilon_0 e} \times \frac{\sigma_2^{abb}}{\mathrm{Im}\epsilon^{bb}}, \tag{1}$$

where $\epsilon^{bb} = 1 + i\sigma_1^{bb}/\epsilon_0\omega$ is the complex dielectric function within the independent-particle approximation, with ϵ_0 the vacuum permittivity and e the electron charge. Since Eq. (1) involves a ratio between the quadratic and linear absorption coefficients, the shift distance has length units and is independent of the slab dimension, allowing a direct comparison of monolayer and nanotube results. In Fig. 3, we show the calculated results of the main component D^{xxx} for the monolayer as well as for single-wall nanotubes for radii ranging from 15 to 60 Å. While the peak structure closely follows that of optical properties in all cases, the shape is significantly altered, showing maxima at ∼3.5 eV. Overall, the calculated shift distance is of the order of the average bond length between S−S and W−S atoms in the monolayer configuration, indicated in the

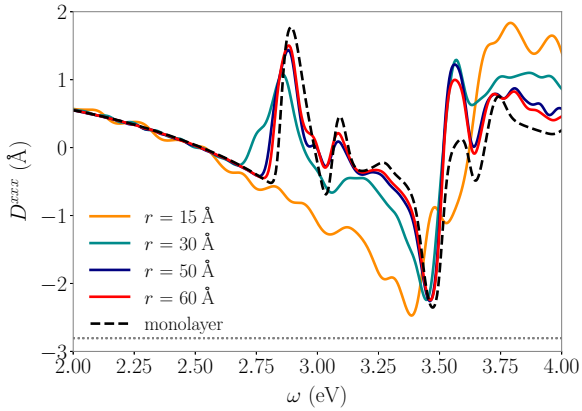

FIG. 3. A plot comparing the shift distance tensor (D^{xxx}) as a function of photon frequency (ω in eV) for nanotubes with varying radii (r) and a monolayer. The monolayer's result is represented by a black dashed line, while the nanotubes are indicated by colored lines. The grey dashed line shows the average bond length of 2.8 Å between the ions in the monolayer.

figure. This magnitude is in line with what has been previously reported in bulk materials [39,40].

We end this section by inspecting the dependence of the shift distance on the nanotube radius. For a nanotube with $r = 15$ Å, we find no peak at ∼2.9 eV and the shape of D^{xxx} deviates significantly from the monolayer result. However, as r is increased, the nanotube shift distance tends to match the shape as well as magnitude of the monolayer result; for $r = 60$ Å, only slight deviations are visible. This is an important result, as it shows that nanotubes with radius larger than 60 Å fall within the monolayer limit. Given that, in reality, all walls of synthesized nanotubes have $r > 60$ Å [41,42], their optical properties can be conveniently described by those of the monolayer, provided interwall interactions are not too large. The latter are analyzed in the following section.

2. *Double-wall nanotube*

Here we report on the linear and shift photoconductivity of a double-wall WS_2 nanotube; see Fig. 4(a) for a schematic illustration. For their construction, we stacked two single-wall zigzag nanotubes of different radii on one another. In our calculations, we have fixed the radius of the inner wall at $r = 30$ Å and varied the radius of the outer wall to sample the photoresponse for varying interwall distance h. The interwall distance in the ideal WS_2 bilayer structure is $h \approx 6.23$ Å, which increases by ∼2% in nanotubes [41,43]. Having this in mind, in Figs. 4(b)–4(e) we show the calculated $\sigma_1^{xx}(\omega)$ and $\sigma_2^{xxx}(\omega)$ for $h = 6$ Å, 6.5 Å and 7 Å. In addition to the double-wall results, we have also included results corresponding to the individual constituent walls, hence the difference between the two sets can be attributed to the interwall interaction.

Figures 4(b) and 4(c) for $h = 6$ Å show that, while the interwall interaction induces visible deviations from the single wall result, it does not alter the order of magnitude of the optical responses. The largest effect on the shift current takes place at 2.9 eV, where the peak of the double-wall result flips the sign. However, already for $h = 6.5$ Å [Figs. 4(d) and 4(e)] the interwall interaction induces only minor differences with respect to the single wall result, and the main spectral features are practically restored. Given that synthesized WS_2 nanotubes are likely to have an interwall distance closer to 6.5 Å than 6.0 Å, our calculations indicate that the interwall interaction does not affect the photoresponse properties to the extent that it could explain the enhancement reported in the experiment of Ref. [19]. We have verified that this holds for different rotation angles of one wall with respect to the other [see Figs. 4(h) and 4(i)] as well as for other values of the inner and outer walls (keeping the considered range of interwall distance).

The above results are in apparent contrast to some of the results reported in Ref. [20], where an acute enhancement of the shift photoconductivity (but not of the linear absorption) was observed in double-wall nanotubes with interwall distance around 6 Å, which was attributed to a wall-to-wall charge shift. We have not found evidence of this enhancement in our calculations, even when using the same radii reported in Ref. [20]. We note that, unlike in the theoretical approach employed in Ref. [20], we do not resort to a tight-binding model derived from Wannier functions as we keep the whole matrix structure of both the Hamiltonian as well as the position matrix elements [21]. This might explain part of the difference with the results of that work, given that position matrix elements can play an important role in the shift-current generation [44].

C. Total current: Monolayer versus nanotube

1. *Estimates of relevant quantities*

We turn now to analyze the factors involved in the generation of the total shift current of WS_2 monolayer and nanotube. For a material with thickness d, the shift current generated under linearly polarized light $\mathbf{E}$ in a direction normal to the incidence can be written as [45]

$$J_a = G^{abb}(\omega) \cdot [1 - R(\omega)] \cdot (1 - e^{-\alpha_{bb}(\omega)\cdot d}) \cdot w \cdot I_b, \qquad (2)$$

with $I_b = c\epsilon_0 E_b^2/2$ and c the speed of light. There are several quantities entering the above expression, which we now discuss one by one in the context of the experimental setup of Ref. [19].

The factor $1 - R(\omega)$ describes the portion of light that is not reflected at the surface between the vacuum and the material. It involves the *reflectivity*

$$R(\omega) = \frac{[1 - n(\omega)]^2 + \kappa(\omega)^2}{[1 + n(\omega)]^2 + \kappa(\omega)^2}, \qquad (3)$$

where the coefficients n and κ are related to the real (R) and imaginary (I) parts of the complex dielectric function $\epsilon^{bb} = \epsilon_{\mathrm{R}}^{bb} + i\epsilon_{\mathrm{I}}^{bb}$ as $\epsilon_{\mathrm{R}}^{bb} = n^2 - \kappa^2$ and $\epsilon_{\mathrm{I}}^{bb} = 2n\kappa$. In Fig. 5(b), we show the calculated reflectivity factor $R(\omega)$. It shows that, at the band edge, approximately half the incoming light is reflected, whereas at the peak energy $\omega \simeq 2.9$ eV, approximately 70% of light is reflected; both these values are in rather good agreement with the experimental measurements of Ref. [46], which we have reproduced in the figure. Given that the reflectivity is mainly a surface property, we assume that the same factor applies to the monolayer and the nanotube. This is backed up by a recent experiment on WS_2 nanotubes

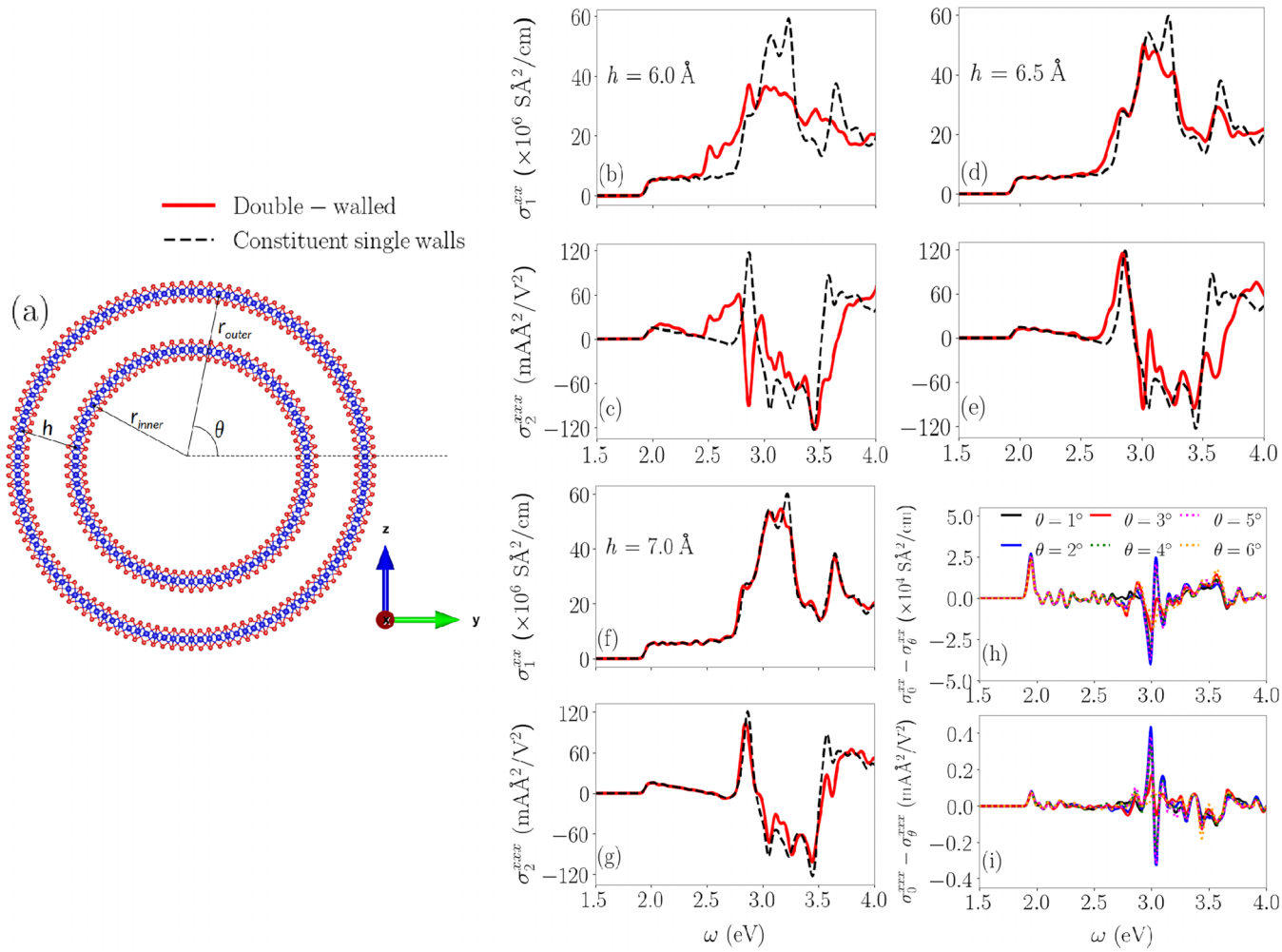

FIG. 4. (a) Side view of a double-wall nanotube defined by its inner radius (r_{inner}), outer radius (r_{outer}), and the distance between the walls (h). The chirality of the inner wall is fixed at (60,0) and we varied the outer in the range (72,0), (73,0), and (74,0) to maintain interlayer distances of 6.0 Å, 6.5 Å, and 7.0 Å, respectively. The angle θ signifies the rotational displacement of the outer wall relative to the inner wall. (b)–(g) The linear and shift current photoresponses of the double-wall nanotubes having interwall distances of $h \in [6, 6.5, 7]$ Å (red solid lines). These are compared with responses of the individual single-wall nanotubes constituting a double wall (black dashed lines). (d), (e) The photoresponse for $h = 6.5$ Å which is closest to the interwall distance of WS_2 nanotubes [41,43]. (h), (i) Depiction of how the photoresponses are affected when the outer wall is rotated with respect to the inner wall by angle θ in range $\in [1^\circ - 6^\circ]$ (for higher angles, the structure repeats). Here, we have shown the results for a smaller double wall nanotube with $r_{\text{inner}} = 30$ Å, $r_{\text{outer}} = 37$ Å, and $h = 6.5$ Å.

and 2D sheets, which displays very similar levels of reflection intensity for most frequencies [47].

The factor I_b in Eq. (2) accounts for the intensity of the electric field. Reference [19] employed a Gaussian beam, and for a laser of 632.8 nm wavelength, the average electric field strength (or power density) over the spot size is 1.39×10^4 W/cm^2. This number appropriately describes the action of the electric field over the monolayer, given that its dimensions described by $L = 2$ μm are of the order of the spot-size diameter $H = 2.5$ μm [19] (see Fig. 6 for a sketch). In turn, the effective strength of the electric field acting on the nanotube is larger than the average value, given that it is placed in the middle of the laser spot size where light intensity is highest and its radius $r = 90$ nm is small in comparison to H (see Fig. 6). Considering the Gaussian profile employed in Ref. [19], we find that the effective strength in the nanotube is approximately 15% larger than the average value, hence we use $I_b = 1.6\times10^4$ W/cm^2 for the nanotube.

Finally, we come to analyze the geometric and light-absorption terms in Eq. (2). The symbol w denotes the length of the material exposed to light illumination, which is $w_{\text{M}} = L$ in the case of the monolayer and $w_{\text{NT}} = 2r$ for the nanotube (see Fig. 6). Plugging the numbers, we get that $w_{\text{M}} \simeq 10 \cdot w_{\text{NT}}$, reflecting the fact that the monolayer is much wider than the nanotube diameter. On the other hand, $G^{abb}(\omega)$ in Eq. (2) stands for the *Glass coefficient* [48,49]

$$G^{abb}(\omega) = \frac{2\sigma_2^{abb}(\omega)}{c\epsilon_0\sqrt{\epsilon_r}\cdot\alpha_{bb}(\omega)}, \tag{4}$$

with ϵ_r the dielectric constant of the material. The Glass coefficient thus involves the ratio between the shift current and the *absorption coefficient* [46]:

$$\alpha_{bb}(\omega) = \sqrt{2}\frac{\omega}{c}\sqrt{|\epsilon^{bb}| - \epsilon_{\text{R}}^{bb}}. \tag{5}$$

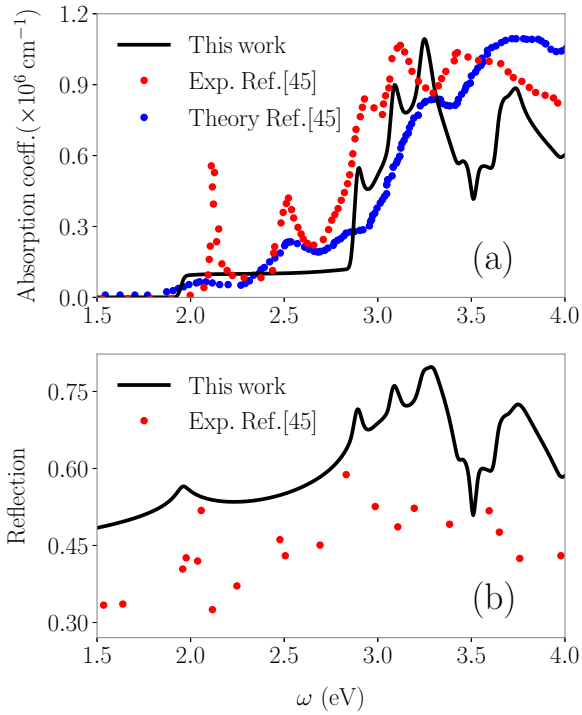

FIG. 5. The plot displays the (a) absorption coefficient and (b) reflection ratio as a function of photon frequency ω (in eV). The solid black line represents our theoretical calculations for the WS_2 monolayer. For comparison with our results, the experimental and theoretical data from Ref. [45] are displayed in the figures as indicated in red and blue dots, respectively. The sharp peaks at ~ 2.2 eV and ~ 2.5 eV correspond to excitons measured in experiment.

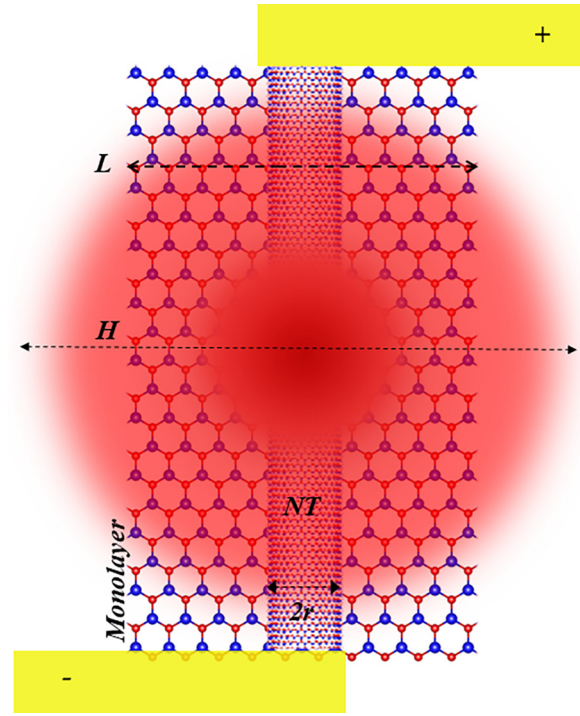

FIG. 6. Schematic diagram showing the experimental setup which we used for estimating the total current flowing through monolayer and nanotube. We have denoted the spot size of the laser profile as H, which is illuminated on a monolayer of width L and a nanotube of radius r. The current flows between the electrodes, which are marked by the terminals $+/-$.

The inverse of the absorption coefficient describes the light penetration depth into the material. We note that, in the limit of thin materials, $\alpha_{bb}^{-1}(\omega) \gg d$, and therefore the expression of Eq. (2) reduces to $J_a = \sigma_2^{abb}(\omega) \cdot [1 - R(\omega)] \cdot d \cdot w \cdot I_b/\sqrt{\epsilon_r}$, which is independent of $\alpha_{bb}(\omega)$ and involves the cross section $d \cdot w$ normal to the flow of current.

In Fig. 5(a), we show the calculated absorption coefficient for WS_2. The figure shows that $\alpha_{bb}(\omega)$ ranges between $\sim 1\times10^5$ cm^{-1} at the band edge and $\sim 5\times10^5$ cm^{-1} at the peak energy $\omega = 2.9$ eV. These values are in good agreement with previously reported experimental measurements and theoretical estimates of $\alpha_{bb}(\omega)$ [45]. In practical terms, this means that the light penetration depth ranges between $\simeq 1000$ Å at the band edge and $\simeq 200$ Å at $\omega = 2.9$ eV. In the case of the monolayer, its thickness $d_M = 3.14$ Å is orders of magnitude smaller than the penetration depth. As for the nanotube, it is typically composed of ~ 25 layers and light traverses them twice in most regions. Considering the interwall distance of $\sim$6.5 Å [41,43], a nanotube is roughly $d_{NT} \simeq 300$ Å thick; given that $d_{NT} \lesssim \alpha_{bb}^{-1}(\omega)$, most layers of the nanotube are active in absorbing light. This, in turn, means that $d_{NT} \simeq 100 \cdot d_M$, reflecting the fact that a nanotube is much "thicker" than a monolayer. Combining with the width factor discussed earlier, we conclude that $w_{NT} \cdot d_{NT} \simeq 10 \cdot w_M \cdot d_M$, which represents roughly an order of magnitude enhancement of the nanotube as compared to the monolayer.

2. *Angular dependence and magnitude of the photocurrent*

As the last step in our analysis, we study the angular dependence of the shift photocurrent in the two structures based on the arguments of the preceding sections and quantitatively compare our results to the experimental measurements of Ref. [19]. We assume linearly polarized light in the xy plane under normal incidence, with its electric field described by

$$\mathbf{E}(\omega) = E(\omega)(\cos\theta\hat{i} + \sin\theta\hat{j}). \tag{6}$$

The total current generated along the x axis can then be expressed as

$$J^x(\theta, \omega) = A \cdot (G^{xxx}(\omega)\cos^2\theta + G^{xyy}(\omega)\sin^2\theta), \tag{7}$$

where $A = [1 - R(\omega)] \cdot (1 - e^{-\alpha_{bb}(\omega)\cdot d}) \cdot w \cdot I_b$ gathers the remaining factors of Eq. (2).

To illustrate our results, in Fig. 7 we have considered two photon energies; 2 eV, where Ref. [19] measured maximum current, and 2.9 eV, where our calculations predict maximum shift photoconductivity (see Fig. 2). Let us begin by discussing the monolayer results of Fig. 7(a). Our calculations predict a photocurrent smaller than 0.1 nA for photon energy 2 eV, while at 2.9 eV it is maximum and of the order of 1 nA. To put this into context, $BaTiO_3$ reaches a maximum shift current of 6×10^{-3} nA [9,10]. As for the measurements performed in monolayer WS_2, Ref. [19] did not report a photocurrent larger than 0.1 nA. This suggests that either our calculations overestimate the peak shift-current value by at least an order of magnitude or some other effect counteracts

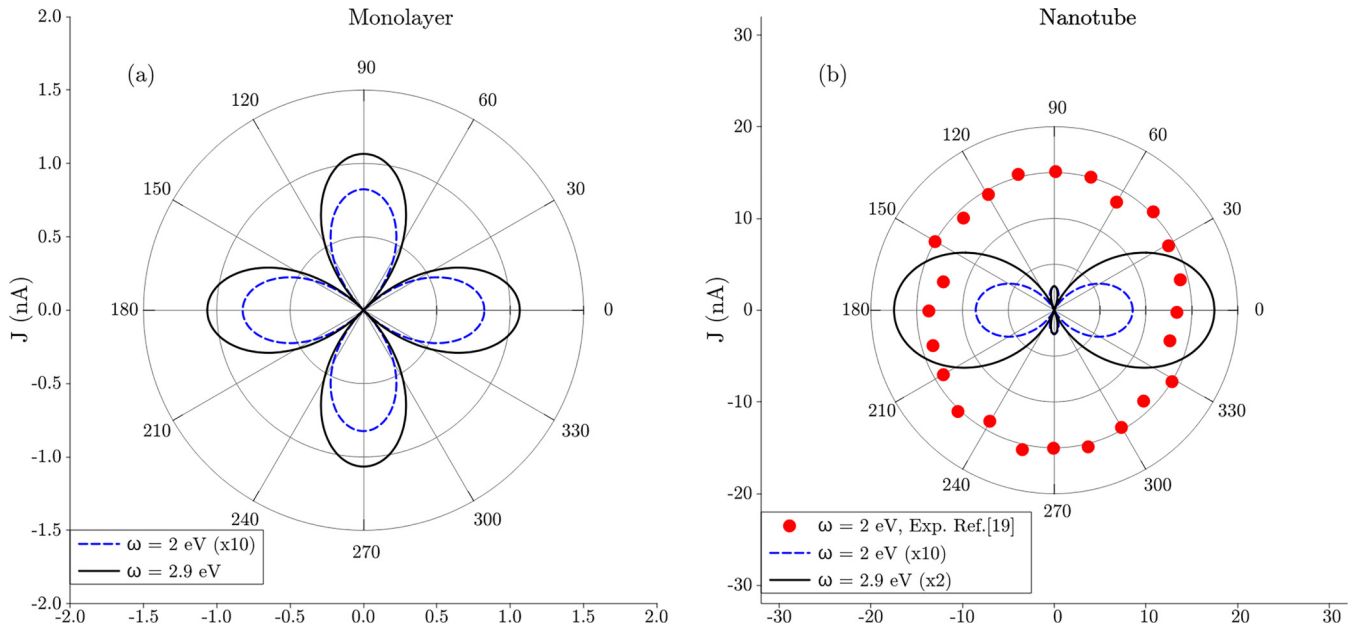

FIG. 7. Polar plot showing the variation of shift current (J) in nA as a function of the polarization angle θ at normal incidence for WS_2 (a) monolayer and (b) nanotube. The excitation energies $\omega = 2$ eV and 2.9 eV correspond to the response at the band edge and peak, respectively. The nanotube's result is compared with the experimental data of device1 ($r = 90$ nm) [19] (red dots).

its contribution. Such an effect could be the so-called *ballistic current* [2,50] and extrinsic kinetic contribution to the BPVE that can be as large or even larger than the shift current [51]. In any case, except for the peak magnitude our results on the monolayer are not inconsistent with the experimental findings of Ref. [19], given that in most spectral regions our calculations predict a shift current smaller than 0.1 nA.

We come next to the nanotube results shown in Fig. 7(b); in our calculations, we have disregarded interwall interactions and employed the photoconductivity of a single-wall nanotube with $r = 60$ Å, together with $d = 300$ Å in Eq. (2), corresponding to a typical nanotube composed of $N = 25$ layers [19,41]. The calculated nanotube photocurrent in Fig. 7(b) ranges between order 1 nA at 2 eV and 10 nA at 2.9 eV, showing an elongated shape around $\theta = 0$ owing to the dominance of σ^{xxx} over σ^{xyy} (see Fig. 2). The maximum photocurrent measured in Ref. [19] is also of the order of 10 nA, but takes place at 2 eV, coinciding with the energy of the so-called A exciton of WS_2. Aside from the mismatch in energy, our calculations show that a zigzag WS_2 nanotube with shift photoconductivity equal to the monolayer can account for the order of magnitude measured in Ref. [19]. As for the angular dependence, the measured data for the nanotube shows a rounded shape around the origin, but this distribution appears to depend significantly on the precise nanotube that is measured [19].

We note that the nanotubes used in experiment are typically composed of a mixture of internal structures (i.e., zigzag, armchair, and chiral) that is, in general, unknown, and even the radius is not constant throughout the whole nanotube, hence significant deviations from our idealized results are to be expected. Improved theoretical results could be obtained by the modeling of interfaces between different types of structures. Considering many-body interactions in the quadratic photoresponse [16,17,52–54] could also bring numerical results closer to experiment. In particular, TMDs host the so-called A and B excitons [18] that translate into narrow peaks in the spectra (see Fig. 5) which are not captured in our current theoretical description. The few available theoretical works reporting excitonic contributions to the shift current indicate that the effect can be significant [16,17,53,55]. We expect to tackle these aspects in future work.

IV. CONCLUSIONS

In summary, we have conducted a systematic study of the shift current in WS_2 monolayer and nanotube structures. Our DFT calculations have shown that the optical properties of a single wall zigzag nanotube are well described by those of a monolayer for nanotube radius larger than ∼60 Å. According to our calculations, the single-wall results are only slightly modified when accounting for interactions with other walls of the nanotube for typical interwall distances. Despite possessing a similar shift photoconductivity, we have shown that a WS_2 nanotube can generate a photocurrent of around 10 nA, while the monolayer attains a maximum photocurrent of order 1 nA. The main reason behind this difference is the larger conducting cross section of a nanotube in comparison to a monolayer. Our calculations reproduce the order of magnitude of the photocurrent measured in a recent experiment on WS_2 nanotubes [19], suggesting that the shift current plays an important role.

ACKNOWLEDGMENTS

We are very grateful to Y. Zhang for stimulating correspondence. This project has received funding from the European Union's Horizon 2020 research and innovation program under the European Research Council (ERC) Grant Agreement No. 946629, and the Department of Education, Universities and

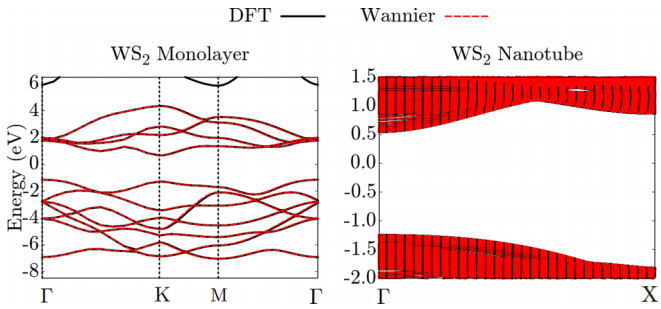

FIG. 8. The DFT (in solid black line) and Wannier-interpolated (in dashed red line) band structure of monolayer and nanotube. The Fermi energy level is set at 0 eV.

Research of the Eusko Jaurlaritza, and the University of the Basque Country UPV/EHU (Grant No. IT1527-22).

APPENDIX: ADDITIONAL CALCULATIONS

Here we provide additional calculations on electronic structure and optical properties.

1. Band structure and Wannier interpolation

Figure 8 shows the calculated band structure for WS_2 monolayer [Fig. 1(b)] and zigzag nanotube of radius $r = 40$ Å [Fig. 1(a)]. We have also included the Wannier-interpolated band structure, which reproduces the DFT one. The figure shows that the direct band gap of the monolayer takes place at high-symmetry point K, while in the nanotube it takes place at Γ. The value of the band gap is $\simeq 2$ eV, virtually the same in both structures

2. Shift current

a. Atomic relaxation

In the calculations in the main text, we considered ideal (unrelaxed) atomic positions for the nanotubes. The reason to proceed in this way is twofold. First, we have checked that the relaxation procedure results in changes of the bond lengths below 1%; this implies that the shift current is only mildly affected as compared to the ideal structure, as exemplified in Fig. 9(a) for a zigzag nanotube of $r = 40$ Å. In all calculations, the computed static stress is <0.01 eV/Å^3. Second, working with the ideal atomic structure makes sure that the monolayer and nanotube geometries are as close as possible. This then allows a clear comparison of the optical properties of a monolayer and the corresponding nanotube constructed from it, better highlighting the similarities and differences between them.

b. Spin-orbit coupling

Spin-orbit coupling (SOC) is usually not the main driving effect for the shift current of semiconductors. However, given

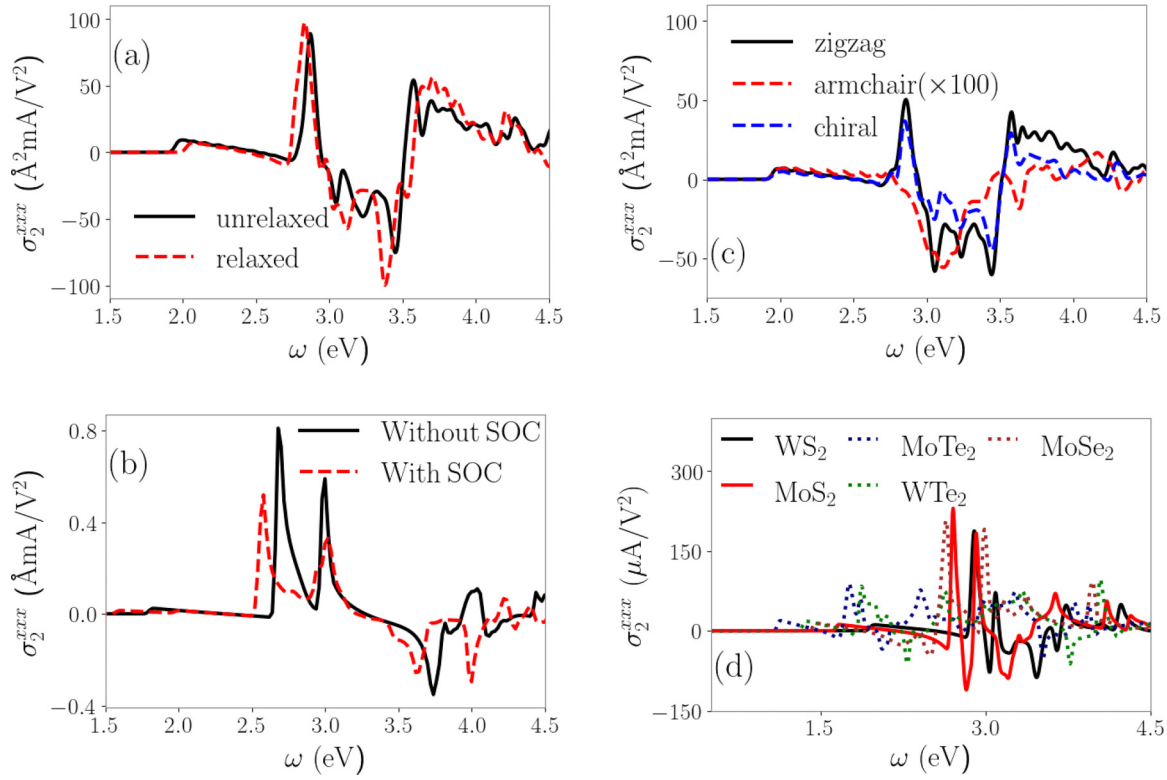

FIG. 9. Dominant tensor component of shift photoconductivity σ_2^{xxx} as a function of frequency for various cases. (a) Unrelaxed (black line) and relaxed (red line) structure of a zigzag WS_2 nanotube of $r = 40$ Å. (b) Calculations in monolayer WS_2 with and without spin-orbit coupling as shown in red dashed and black solid line, respectively. (c) Zigzag (in black solid), armchair (in red dashed), and chiral (in blue dashed) nanotube configurations of $r = 30$ Å. The chiral angle for the chiral nanotube is 16.102°. (d) Several MX_2 combinations ($M =$ Mo/W; $X =$ S, Te, Se).

that tungsten is a heavy element, we have conducted additional calculations on the shift photoconductivity including SOC. We have conducted these calculations using the plane-wave-based QUANTUM ESPRESSO code package [56], given that the interface to the WANNIER90 code package is currently implemented for the case of fully relativistic pseudopotentials. Figure 9(b) shows the dominant tensor component of the shift photoconductivity σ_2^{xxx} of monolayer WS_2 calculated with and without SOC. The figure shows that the band-gap energy is reduced by $\simeq 0.2$ eV as a consequence of SOC, and the main spectral features are somewhat shifted to lower energies roughly by that amount. As expected, the overall order of magnitude of the shift photoconductivity is not altered by SOC. We have verified that this is also the case for calculations of nanotube structures, and that the main results of this paper are also not modified by SOC.

c. Nanotube configurations

In addition to the zigzag configuration, an experimentally synthesized TMD nanotube can coexist with two other configurations, namely, armchair (n, n) and chiral (n, m). In Fig. 9(c), we present a comparative analysis of the dominant tensor of the shift photoconductivity σ_2^{xxx} of three different WS_2 nanotube configurations, namely, zigzag, armchair, and chiral, each with a radius of 30 Å. The figure shows that σ_2^{xxx} for the armchair configuration is two orders of magnitude smaller as compared to the zigzag. On the other hand, the shift current of chiral nanotubes follows the same peak trend and the same order of magnitude as the zigzag.

d. Different TMDs

Finally, we have extended the calculations to cover the TMD combinations $M =$ Mo, W and $X =$ S, Se, Te. Figure 9(d) shows the calculated σ_2^{xxx} (including SOC) of the monolayer structure for all these combinations. As shown by the figure, the overall order of magnitude is the same for all the TMDs, with a maximum shift photoconductivity of 220 $\mu A/V^2$ attained in MoS_2.

[1] B. I. Sturman and V. M. Fridkin, *The Photovoltaic and Photorefractive Effects in Noncentrosymmetric Materials*, 1st ed. (Routledge, London, 2021).
[2] V. M. Fridkin, Cryst. Rep. **46**, 654 (2001).
[3] J. E. Spanier, V. M. Fridkin, A. M. Rappe, A. R. Akbashev, A. Polemi, Y. Qi, Z. Gu, S. M. Young, C. J. Hawley, D. Imbrenda *et al.*, Nat. Photon. **10**, 611 (2016).
[4] G. B. Osterhoudt, L. K. Diebel, M. J. Gray, X. Yang, J. Stanco, X. Huang, B. Shen, N. Ni, P. J. Moll, Y. Ran *et al.*, Nat. Mater. **18**, 471 (2019).
[5] S. M. Young, F. Zheng, and A. M. Rappe, Phys. Rev. Lett. **109**, 236601 (2012).
[6] Y. Zhang, T. Holder, H. Ishizuka, F. de Juan, N. Nagaosa, C. Felser, and B. Yan, Nat. Commun. **10**, 3783 (2019).
[7] J. Ma, Q. Gu, Y. Liu, J. Lai, P. Yu, X. Zhuo, Z. Liu, J.-H. Chen, J. Feng, and D. Sun, Nat. Mater. **18**, 476 (2019).
[8] M.-M. Yang, D. J. Kim, and M. Alexe, Science **360**, 904 (2018).
[9] W. Koch, R. Munser, W. Ruppel, and P. Würfel, Solid State Commun. **17**, 847 (1975).
[10] S. M. Young and A. M. Rappe, Phys. Rev. Lett. **109**, 116601 (2012).
[11] A. M. Cook, B. M. Fregoso, F. De Juan, S. Coh, and J. E. Moore, Nat. Commun. **8**, 14176 (2017).
[12] T. Rangel, B. M. Fregoso, B. S. Mendoza, T. Morimoto, J. E. Moore, and J. B. Neaton, Phys. Rev. Lett. **119**, 067402 (2017).
[13] J. Y. Kwak, Results Phys. **13**, 102202 (2019).
[14] M. Bernardi, M. Palummo, and J. C. Grossman, Nano Lett. **13**, 3664 (2013).
[15] P. Král, E. J. Mele, and D. Tománek, Phys. Rev. Lett. **85**, 1512 (2000).
[16] S. Konabe, Phys. Rev. B **103**, 075402 (2021).
[17] Y.-S. Huang, Y.-H. Chan, and G.-Y. Guo, Phys. Rev. B **108**, 075413 (2023).
[18] K. M. McCreary, A. T. Hanbicki, S. V. Sivaram, and B. T. Jonker, APL Mater. **6**, 111106 (2018).
[19] Y. J. Zhang, T. Ideue, M. Onga, F. Qin, R. Suzuki, A. Zak, R. Tenne, J. H. Smet, and Y. Iwasa, Nature (London) **570**, 349 (2019).
[20] B. Kim, N. Park, and J. Kim, Nat. Commun. **13**, 3237 (2022).
[21] J. Ibañez-Azpiroz, S. S. Tsirkin, and I. Souza, Phys. Rev. B **97**, 245143 (2018).
[22] J. M. Soler, E. Artacho, J. D. Gale, A. García, J. Junquera, P. Ordejón, and D. Sánchez-Portal, J. Phys.: Condens. Matter **14**, 2745 (2002).
[23] W. E. Pickett, Comput. Phys. Rep. **9**, 115 (1989).
[24] D. R. Hamann, M. Schlüter, and C. Chiang, Phys. Rev. Lett. **43**, 1494 (1979).
[25] D. M. Ceperley and B. J. Alder, Phys. Rev. Lett. **45**, 566 (1980).
[26] J. P. Perdew and A. Zunger, Phys. Rev. B **23**, 5048 (1981).
[27] W. Schutte, J. De Boer, and F. Jellinek, J. Solid State Chem. **70**, 207 (1987).
[28] I. Souza, N. Marzari, and D. Vanderbilt, Phys. Rev. B **65**, 035109 (2001).
[29] N. Marzari and D. Vanderbilt, Phys. Rev. B **56**, 12847 (1997).
[30] G. Pizzi, V. Vitale, R. Arita, S. Bluegel, F. Freimuth, G. Géranton, M. Gibertini, D. Gresch, C. Johnson, T. Koretsune, Ibañez-Azpiroz, H. Lee, J.-M. Lihm, D. Marchand, A. Marrazzo, Y. Mokrousov, J. I. Mustafa, Y. Nohara, Y. Nomura, L. Paulatto *et al.*, J. Phys.: Condens. Matter **32**, 165902 (2020).
[31] J. E. Sipe and A. I. Shkrebtii, Phys. Rev. B **61**, 5337 (2000).
[32] X. Wang, J. R. Yates, I. Souza, and D. Vanderbilt, Phys. Rev. B **74**, 195118 (2006).
[33] M. Damnjanović, T. Vuković, and I. Milošević, Isr. J. Chem. **57**, 450 (2017).
[34] J.-Q. Hu, X.-H. Shi, S.-Q. Wu, K.-M. Ho, and Z.-Z. Zhu, Nanoscale Res. Lett. **14**, 288 (2019).
[35] F. Zheng, H. Takenaka, F. Wang, N. Z. Koocher, and A. M. Rappe, J. Phys. Chem. Lett. **6**, 31 (2015).
[36] J. A. Brehm, S. M. Young, F. Zheng, and A. M. Rappe, J. Chem. Phys. **141**, 204704 (2014).

[37] M. Staiger, P. Rafailov, K. Gartsman, H. Telg, M. Krause, G. Radovsky, A. Zak, and C. Thomsen, Phys. Rev. B **86**, 165423 (2012).
[38] N. Zibouche, A. Kuc, and T. Heine, Eur. Phys. J. B **85**, 49 (2012).
[39] F. Nastos and J. E. Sipe, Phys. Rev. B **74**, 035201 (2006).
[40] J. Ibañez-Azpiroz, I. Souza, and F. de Juan, Phys. Rev. Res. **2**, 013263 (2020).
[41] A. Zak, L. Sallacan-Ecker, A. Margolin, Y. Feldman, R. Popovitz-Biro, A. Albu-Yaron, M. Genut, and R. Tenne, Fullerenes, Nanotubes Carbon Nanostruct. **19**, 18 (2010).
[42] F. Qin, W. Shi, T. Ideue, M. Yoshida, A. Zak, R. Tenne, T. Kikitsu, D. Inoue, D. Hashizume, and Y. Iwasa, Nat. Commun. **8**, 14465 (2017).
[43] V. Brüser, R. Popovitz-Biro, A. Albu-Yaron, T. Lorenz, G. Seifert, R. Tenne, and A. Zak, Inorganics **2**, 177 (2014).
[44] J. Ibañez-Azpiroz, F. de Juan, and I. Souza, SciPost Phys. **12**, 070 (2022).
[45] R. Fei, L. Z. Tan, and A. M. Rappe, Phys. Rev. B **101**, 045104 (2020).
[46] H.-L. Liu, T. Yang, J.-H. Chen, H.-W. Chen, H. Guo, R. Saito, M.-Y. Li, and L.-J. Li, Sci. Rep. **10**, 15282 (2020).
[47] Z. Liu, A. W. A. Murphy, C. Kuppe, D. C. Hooper, V. K. Valev, and A. Ilie, ACS Nano **13**, 3896 (2019).
[48] A. Glass, D. Von der Linde, and T. Negran, Appl. Phys. Lett. **25**, 233 (1974).
[49] L. Z. Tan, F. Zheng, S. M. Young, F. Wang, S. Liu, and A. M. Rappe, npj Comput. Mater. **2**, 16026 (2016).
[50] V. I. Belinicher, E. L. Ivchenko, and B. Sturman, Zh. Eksp. Teor. Fiz. **83**, 649 (1982) [Sov. Phys. JETP **56**, 359 (1982)].
[51] B. I. Sturman, Phys. Usp. **63**, 407 (2020).
[52] E. Luppi, H. Hübener, and V. Véniard, Phys. Rev. B **82**, 235201 (2010).
[53] Y.-H. Chan, D. Y. Qiu, F. H. da Jornada, and S. G. Louie, Proc. Natl. Acad. Sci. **118**, e1906938118 (2021).
[54] P. Garcia-Goiricelaya, J. Krishna, and J. Ibañez-Azpiroz, Phys. Rev. B **107**, 205101 (2023).
[55] A. Taghizadeh and T. G. Pedersen, Phys. Rev. B **97**, 205432 (2018).
[56] P. Giannozzi, O. Andreussi, T. Brumme, O. Bunau, M. B. Nardelli, M. Calandra, R. Car, C. Cavazzoni, D. Ceresoli, M. Cococcioni *et al.*, J. Phys.: Condens. Matter **29**, 465901 (2017).